Subpercent-Scale Control of 3-D Modes 1, 2, and 3 of Targets Imploded in a Direct-Drive Configuration on OMEGA

In laser-driven implosion experiments, a laser illuminates a spherical target either directly (direct-drive configuration) or after conversion into x rays (indirect-drive configuration). This absorbed laser energy leads to the ablation and extreme acceleration of the outer surface of the target through the "rocket effect." This method is widely used to study plasma physics[1] including high-energy-density physics[2–4] and inertial confinement fusion (ICF).[5] In all cases, maintaining spherical symmetry throughout the implosion is critical to obtaining a 1-D behavior that maximizes the internal energy of the imploded plasma at final compression. In ICF experiments, a capsule filled with deuterium (D) and tritium (T) is used to create a self-sustained fusion burn that will ignite the fuel and produce a net energy gain. At the end of the implosion, the kinetic energy of the imploding capsule is converted into internal energy, triggering the fusion reaction during stagnation. Several simulations and comparisons with experiments have shown that target low-mode nonuniformities lead to a severe reduction in the implosion performance because of increased residual kinetic energy during stagnation and uneven compression that result in reduced core pressure and truncated burn.[6–9] This degradation was shown to be particularly significant for modes $\ell \leq 3$, where ℓ is the order of the modes of the spherical harmonic decomposition of the shell's shape.[8,10] Consequently, reducing low-mode nonuniformity has been identified as one of the most-critical steps in demonstrating ignition at the National Ignition Facility (NIF)[11–13] or conditions that are hydrodynamically equivalent to ignition when scaled from 26-kJ implosions on OMEGA to megajoule energies on the NIF.[14–16]

Over the last decade, many studies have shown significant low-mode asymmetries of the imploding shell. Modes $\ell = 1$ have been typically identified from properties of the final assembly including asymmetry in its areal density,[17] variation of its ion temperature along different lines of sight,[18] hot-spot motion,[19] and asymmetric x-ray emission of a Ti layer embedded at the inner surface of the shell.[20] Modes $\ell \geq 2$ have been measured from the hot-spot shape,[21,22] standard[23] or Compton[24] radiography, x-ray absorption spectroscopy,[25] and self-emission shadowgraphy.[26]

Several studies have focused on the causes of the asymmetries and the development of methods to correct them. In indirect-drive ICF, the laser's beam-energy balance was modified to exploit cross-beam energy transfer and improve the sphericity of the core emission.[21,22] The improvement was limited, however, because the observable (i.e., the core shape) was restricted to modes $\ell \geq 2$ and too indirect to give accurate access to the 3-D structure of the shell.[10] In direct-drive ICF,[27] simulations have identified different potential effects that create nonuniformities including target offset, beam-power imbalance, beam pointing, and beam timing. Success has been limited, however, in reproducing the experimental observables obtained on OMEGA[28] because of the difficulty in evaluating and modeling each effect.

This article reports the first experimental demonstration that the amplitude of modes $\ell = 1$, 2, and 3 of targets imploded in direct-drive configuration on OMEGA measured at a convergence ratio of ~3 can be controlled within ±0.25% by adjusting the laser's beam-energy balance, leading to a total radial error of 1%. Over three shots, the 3-D shape of the imploding target was tomographically recorded by measuring four lines of sight of the ablation front. The projected ablation-front contours were measured with framing cameras using the x-ray self-emission shadowgraphy technique.[26,29] The projected ablation-front motions were obtained by comparing the positions of the contours on the framing cameras with the corresponding contour positions measured on a nonimploding solid-CH-ball shot. The amplitudes of the modes were determined within ±0.15% by decomposing the contours oriented perpendicular to the lines of sight and shifted by the measured motions over spherical harmonics. The variations of the normalized target mode amplitudes (Δr_ℓ^m, where m is the mode order) between shots were shown to change linearly (within ±0.25%) with the variation of the normalized mode amplitudes of the laser's beam-energy balance $\left(\Delta e_\ell^m\right)$ with a low-mode coupling coefficient $\left(C_\ell = \Delta r_\ell^m \big/ \Delta e_\ell^m\right)$ of $C_1 = -0.66 \pm 0.05$, $C_2 = -0.38 \pm 0.05$, and $C_3 = -0.18 \pm 0.03$ for modes $\ell = 1$, 2, and 3, respectively. The decrease of C_ℓ with increasing mode number was expected because of the phase plates used with each beam on OMEGA.

Lateral thermal transport and amplification by the Rayleigh–Taylor instability were not expected to be important because of the long spatial wavelength ($\lambda = 2\pi R/\ell$, where R is the averaged shell radius) of the low modes. The C_ℓ values enabled one to evaluate within ±0.05% of the amplitudes of the residual target modes that appear when the laser's beam energies are balanced and to determine the laser mode amplitudes that mitigate them within ±0.25%.

The experiments employed 60 ultraviolet ($\lambda_0 = 351$ nm) laser beams on the OMEGA Laser System.[30] The beams illuminated the target and were smoothed by polarization smoothing,[31] smoothing by spectral dispersion,[32] and distributed phase plates (fourth-order super-Gaussian with 95% of the energy contained within the initial target diameter).[33] A 2-ns-long square pulse irradiated 866±3-μm-diam capsules with an energy of 20.2±0.4 kJ, resulting in an intensity $\approx 4.3 \times 10^{14}$ W/cm^2. The shells were made of 19.2±0.2-μm-thick glow-discharge polymer (CH with a density of 1.03 mg/cm^3 and each mode amplitude <50 nm) and filled with 17±1.5 atm of deuterium. An additional reference shot was made on an 856-μm-diam solid CH ball. For each shot, the target was placed at target chamber center with a maximum radial error of 1.5 μm measured with two high-speed video cameras (1000 images per second) that were used to automatically position the target before the shot.

The first shot used a standard laser beam-energy balance with a standard deviation of 2.5%. On the second and third shots, the beam-energy balance was varied to change the amplitude of the evaluated laser modes by minimizing

$$\sum_{b=1}^{60} \left[\sum_{\ell=0}^{\infty} \sum_{m=-\ell}^{\ell} \sqrt{4\pi}\, e_\ell^m Y_\ell^m \left(\theta_b, \phi_b\right) - \bar{E}_b \right]^2$$

with a larger variation for modes $m = 0$, where $\bar{E}_b$ is the energy of the beams normalized to averaged beam energy in percent, (θ_b, ϕ_b) are the coordinates of the OMEGA beam ports, and $Y_\ell^m(\theta, \phi)$ are the tesseral spherical harmonics.[34] On the third shot, one beam was reduced by 80% as a result of hardware malfunction, further amplifying the mode amplitudes. The beam energies were measured with integrated spheres within $\delta\bar{E}_b = \pm0.5\%$ that were absolutely calibrated within ±2% with calorimeters. This resulted in the same relative error for all mode amplitudes of $\delta\left(e_\ell^m\right) = \delta\bar{E}_b / \sqrt{N_b} = \pm0.06\%$, where $N_b = 60$ is the number of beams.

Four x-ray framing cameras, located at different lines of sight, used arrays of 16 pinholes to image the soft x rays emitted by the irradiated target on four strips of a microchannel plate (MCP).[35] The cameras were set up to magnifications of $M = 6$ (two cameras) and $M = 4$ (two cameras) with pinhole sizes of 10 μm and 15 μm, respectively. Their point-spread functions (PSF's) result in about 2-D Gaussian convolutions of the images with a full width at half maximum of $d_{PSF} \approx 10$ μm and $d_{PSF} \approx 15$ μm, respectively.[26] Four short, high-voltage pulses were sent to each strip to activate the signal amplification by the MCP and obtain time-resolved images. For all imploding shells, the electrical pulses were timed to ~0.4 ns, ~1.2 ns, ~1.5 ns, and ~1.8 ns, whereas for the reference shots, they were synchronized to ~0.2 ns after the beginning of the laser pulse (defined as 1% of maximum intensity). The absolute timings between the laser pulse and the images were known to an accuracy of 20 ps, and the interstrip timings were determined within 5 ps (Refs. 26 and 36). Along each strip, the images were separated by ~50 ps. Three cameras had integration times of 40 ps; one had an integration time of 200 ps. On all cameras, 25.4-μm-thick Be filters were used to record the soft x rays above ~1 keV. For each camera, the same pinhole array was used on all shots to maintain the distance between images.

On each self-emission image, the inner edge contour of the intensity peak [Figs. 151.32(a) and 151.32(b)] corresponded to the projection of the ablation-front surface along the line of sight of the diagnostic.[29,37] The recorded intensity was the strongest near the ablation front because the emitting plasma had the largest density (which maximized its emission), and the integration distance of the emitting plasma to the detector was the longest. Just inside the ablation front, the recorded intensity dropped by a factor of 2 over a few microns as the plasma became optically thick, absorbing its emission and the emission coming from the back of the target. The time integration and spatial convolution of the diagnostic induced an inward shift, constant on a given image, of the inner gradient up to 4 μm and 20 μm for integration times of 40 ps and 200 ps, respectively.

The angular variation of the projected ablation-front surface (ΔR_θ) was determined from the difference between the angularly resolved contour radius (R_θ) and the averaged contour radius ($\langle R_\theta \rangle$). To reduce the error, self-emission images were angularly averaged over $\Delta\theta = 20°$, which was larger than the radial convolution $\left[(360/2\pi)\, d_{PSF}/\langle R_\theta \rangle < 5°\right]$ and smaller than the scale length of the modes studied here ($\lambda > 120°$). An error in R_θ of $\delta R_\theta = \pm0.8$ μm was determined on the reference shot by fitting R_θ with a normal distribution and taking the number at the 90th percentile. This error was larger than the error in $\langle R_\theta \rangle$ of $\delta R_\theta / \sqrt{N_{\Delta\theta}} = \pm0.2$ μm, where $N_{\Delta\theta} = 360°/\Delta\theta = 18$ is the number of independent measurements. This resulted in $\delta(\Delta R_\theta) \approx \delta R_\theta$.

On each image, the location of the projected center of the ablation-front surface on the framing camera was determined by finding the center of the circle that minimizes the standard deviation of its radial difference with the contour. This resulted in an accuracy in the center position of $\delta R_{\mathrm{center},1} = \delta R_\theta / \sqrt{N_{\Delta\theta}} = \pm 0.2\ \mu m$. The center location was corrected from the electrical-pulse (EP) propagation that introduced a displacement of the contour along the strip by $-(\Delta R)_{\mathrm{EP}} = VM(\Delta t)_{\mathrm{EP}}$, where V is the implosion velocity, $(\Delta t)_{\mathrm{EP}} = V_{\mathrm{EP}} \langle R_\theta \rangle M$, and V_{EP} is the electrical-pulse velocity that was characterized off-line within $\delta(V_{\mathrm{EP}})/V_{\mathrm{EP}} \pm 10\%$. V was determined by fitting the evolution of $\langle R_\theta \rangle$ linearly for the images of first strip [within $\delta(V)/V = \pm 10\%$] and using a third-order polynomial for the other images [within $\delta(V)/V = \pm 4\%$ (Ref. 26)]. The associated error of

$$\delta R_{\mathrm{center},2} \approx (\Delta R)_{\mathrm{EP}} \left\{ \left[\delta(V)/V \right]^2 + \left[\delta(V_{\mathrm{EP}})/V_{\mathrm{EP}} \right]^2 \right\}^{0.5}$$

grew with time up to $\pm 0.5\ \mu m$. When the images were on the same strip, the error in V_{EP} did not affect the distance between images since it was approximately constant.

The inner edge contours were used to measure the diagnostic magnification on each shot and the magnification anisotropy for each image. On the first strip, the images were recorded at an early time so that the center of the ablation-front surface corresponded to the initial target center, making it possible to measure the diagnostic magnification $M = 1 + D/d$, where D is the distance between contours and $d > 1270\ \mu m$ is the distance between pinholes. This resulted in absolute and relative accuracies of $\approx \delta d/d < \pm 0.005$ and $\approx \sqrt{2}\,\delta R_{\mathrm{center},1} / \left[(M-1)d \right] < \pm 5 \times 10^{-5}$, where $\delta d = \pm 15\ \mu m$ is the error in the pinhole distance specified by the constructor. The error was slightly reduced by linearly fitting D and d over the recorded images. The anisotropy in the camera magnification was determined at each image position on the reference shot by measuring the contour ellipticity. On this shot, all the images were recorded at an early time so the ablation-front nonuniformities were negligible. Although this anisotropy varied among images, it was shown to be consistent at a given image position by repeating the shot.

The shift between each contour center measured on imploding capsule shots and the corresponding contour center measured on the reference shot was used to determine the projected
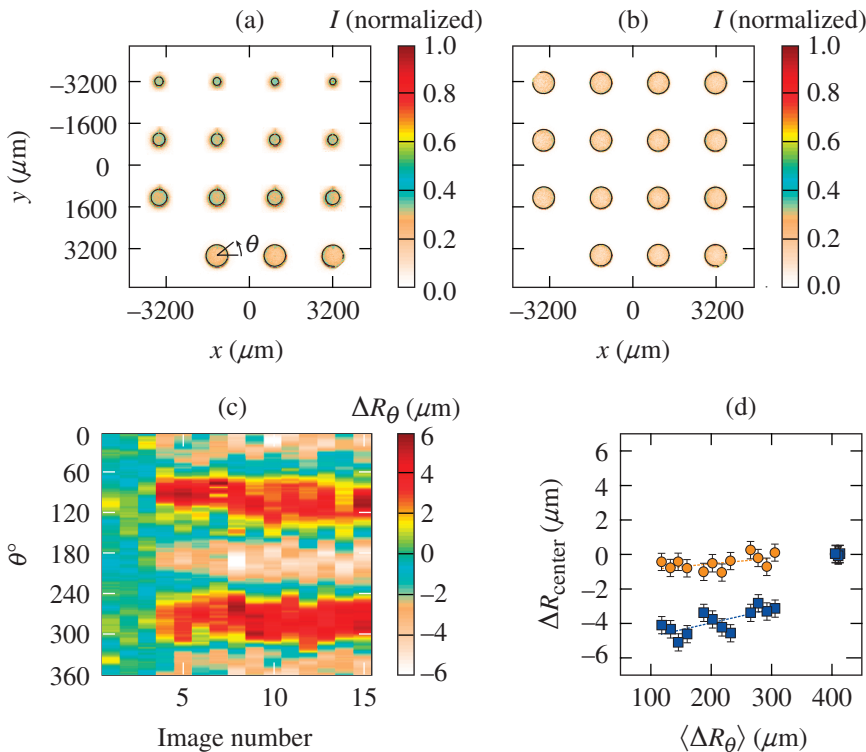

E26367JR

Figure 151.32
Comparison of the self-emission images recorded on (a) the second imploding capsule shot and (b) the reference shot. The circles correspond to the inner edge contours of the intensity peak. (c) Angular variations of the projected ablation-front surface (ΔR_θ) for the images in (a). (d) Projected ablation-front surface motions ($\Delta R_{\mathrm{center}}$) as a function of the averaged contour radius ($\langle\langle R_\theta \rangle\rangle$) along x (orange circles) and y (blue squares) obtained by comparing the contour centers in (a) with the contour centers in (b).

motion of the ablation-front surface (ΔR_{center}). On the reference shot, each contour center corresponded to the projection of the initial target position on the diagnostic. On a capsule implosion, the contour centers determined on the first strip were aligned with the corresponding contour centers measured on the reference shot. This made it possible to correct for differences in diagnostic pointing and initial target position. Longitudinal and transverse differences were accounted for by comparing the diagnostic relative magnifications and the image locations, respectively. The error in ΔR_{center} was given by

$$\delta\left(\Delta R_{\text{center}}\right) \approx \sqrt{2}\left[\delta\left(R_{\text{center},1}\right)^2 + \delta\left(R_{\text{center},2}\right)^2\right]^{0.5} = \pm0.8\ \mu\text{m}.$$

The best estimations of the angular variation of the projected ablation-front surface $(\Delta R_\theta)_{150}$ and motion $(\Delta R_{\text{center}})_{150}$ at an average radius of 150 μm were obtained by linearly fitting their evolution with $\langle R_\theta \rangle$ ranging from ~300 μm to ~100 μm [Figs. 151.32(c) and 151.32(d)]. These evolutions were expected to be linear since, over these radii, there was no significant change in the laser intensity, leading to an almost constant pressure applied to the target: $\Delta R / (\langle R_\theta \rangle - R_0) \approx -\Delta P / \langle P_\theta \rangle \approx -\beta \Delta I / \langle I_\theta \rangle$, where R_0 is the initial target radius; $\langle P_\theta \rangle \propto \langle I_\theta \rangle^\beta$; $\beta \approx 0.5$ (Ref. 15); and ΔR, ΔP, and ΔI are the angular variations and $\langle R_\theta \rangle$, $\langle P_\theta \rangle$, and $\langle I_\theta \rangle$ are the angularly averaged values of the radius, pressure, and laser intensity, respectively. Errors in $(\Delta R_\theta)_{150}$ and $(\Delta R_{\text{center}})_{150}$ of $\delta(\Delta R_\theta)_{150} = \pm0.4\ \mu\text{m}$ and $\delta(\Delta R_{\text{center}})_{150} = \pm0.6\ \mu\text{m}$ at the 90th percentile of the error distribution were determined by comparing ΔR_θ and ΔR_{center} with their linear fits.[38]

The four measured projected contours were oriented perpendicular to the lines of sight of the corresponding framing cameras to determine the 3-D shape of the ablation-front surface [Fig. 151.33(a)]. Because of the 3-D nonuniformities, the center and averaged radii of each contour were slightly different than the center and averaged radius of the 3-D object. To account for this, one contour was used as a reference and the other contours were shifted transversally and magnified to suppress their radial differences with the reference contour at the two crossing points (i.e., where the polar and azimuthal angles are the same).

The 3-D motion of the ablation-front surface was determined by finding the point at the minimum distance between the four lines defined by the lines of sight of the framing cameras shifted by the measured projected motions and by the displacements introduced during the contour alignment process [Fig. 151.33(b)]. The four projected contours provided two measurements each of the three coordinates of the 3-D
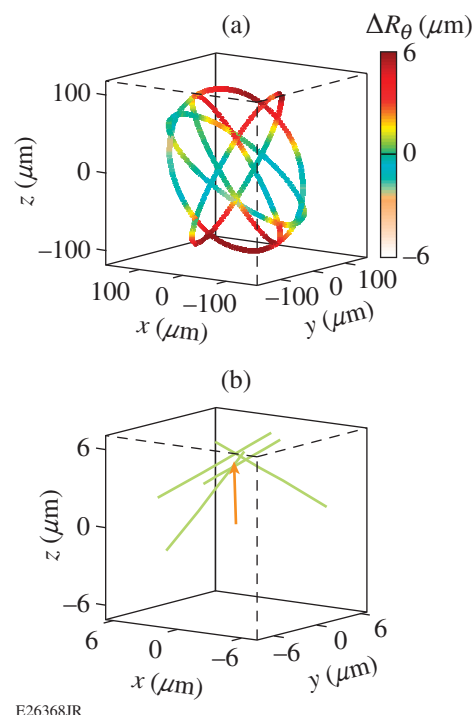

Figure 151.33
(a) The four projected ablation-front contours measured on the second imploding capsule shot were oriented perpendicular to the line of sight of the corresponding framing cameras and then shifted and magnified to minimize the radial difference at the connecting points with the reference contour. (b) The 3-D motion of the ablation-front surface (orange arrow) corresponded to the minimum distance of the four lines (green lines) defined by the lines of sight of each framing camera shifted by the measured projected motions and by the displacements introduced during the contour alignment process.

center, so the five extra measurements reduced the error in the three coordinates.

The amplitudes of modes ℓ = 1, 2, and 3 of the ablation-front surface were obtained by decomposing the four oriented contours shifted by the measured 3-D displacement using spherical harmonics

$$[\bar{R}(\theta_c, \phi_c) = \sum_{\ell=0}^{3} \sum_{m=-\ell}^{\ell} \sqrt{4\pi}\, r_\ell^m Y_\ell^m(\theta_c, \phi_c),$$

where $\bar{R}(\theta_c, \phi_c)$ is the radius normalized to the averaged radius in percent ($r_0^0 = 100\%$) and (θ_c, ϕ_c) are the coordinates of the four contours]. The errors in the mode amplitudes were evaluated by simulating the previously determined error distributions of $\delta(\Delta R_{\text{center}})_{150}$ and $\delta(\Delta R_\theta)_{150}$ and fitting the errors by the normal distribution. Errors of $\delta(r_1^m) = \pm0.15\%$, $\delta(r_2^m) = \pm0.1\%$, and $\delta(r_3^m) = \pm0.1\%$ were obtained at the 90th percentile for modes ℓ = 1, 2, and 3, respectively.

Figures 151.34(a)–151.34(c) show that, for each mode ℓ, the difference in the mode amplitudes of the ablation-front surface between shots Δr_ℓ^m varied linearly with the difference in the corresponding normalized mode amplitudes of the laser's beam-energy balance Δe_ℓ^m with low-mode coupling coefficients of $C_1 = -0.66 \pm 0.05$, $C_2 = -0.38 \pm 0.04$, and $C_3 = -0.18 \pm 0.04$. The negative values were due to the fact that the more intense the laser, the more accelerated that part of the target. The fact that the factor was the same between different shots shows that the effects that create nonuniformities other than the beam-energy balance (such as target position, beam pointing, beam timing) were reproducible between shots. Errors in Δr_ℓ^m of $\delta\left(\Delta r_\ell^m\right) = \pm 0.25\%$, $\delta\left(\Delta r_2^m\right) = \pm 0.3\%$, and $\delta\left(\Delta r_1^m\right) = \pm 0.3\%$ at the 90th percentile were obtained by comparing the points with their linear fits. These comparisons were also used to determine the errors at the 90th percentile of C_ℓ.

The decrease of C_ℓ with mode number [Fig. 151.34(d)] was caused by the phase plates that reduced the amplitude of the modes on target.[39] The laser mode on target is given by

$$\tilde{E}(\theta,\phi) = \sum_{\ell=0}^{\infty}\sum_{m=-\ell}^{\ell}\sqrt{4\pi}\,\tilde{e}_0^0 Y_\ell^m(\theta,\phi),$$

where $\tilde{e}_\ell^m = a_\ell \sum_{b=1}^{60} \bar{E}_b Y_\ell^m(\theta_b,\phi_b) \approx a_\ell e_\ell^m$; a_ℓ are coefficients that describe the profile of each beam,

$$\tilde{E}_b(\theta,\phi) = \bar{E}_b \sum_{\ell=1}^{\infty} a_\ell (2\ell+1)\big/4\pi P_\ell(\cos\gamma)$$

normalized to have $\tilde{e}_0^0 = 100\%$, P_ℓ is the Legendre polynomials, and γ is the angle between (θ, ϕ) and (θ_b, ϕ_b). The SG5 phase plates reduced the values of modes 1, 2, and 3 by factors of 0.79, 0.47, and 0.2, respectively, which result in a constant $C_\ell/a_\ell = 0.85 \pm 0.07$ that relate the laser modes on target to the target modes [Fig. 151.34(d)].

The values of $C_\ell/a_\ell = \Delta R/\langle R_\theta\rangle \times \langle I_\theta\rangle/\Delta I$ resulted in

$$\beta \approx -150\big/(150-R_0) \times C_\ell/a_\ell \approx 0.44 \pm 0.035,$$

which was close to the theoretical value of 0.5. This shows that the smoothing of the laser modes by the lateral heat transport[40] and the amplification by the Rayleigh–Taylor instability were negligible for those modes, as expected.

These linear evolutions allowed us to determine the residual target mode amplitudes $\left[(r_{res})_\ell^m\right]$ that remain when the laser
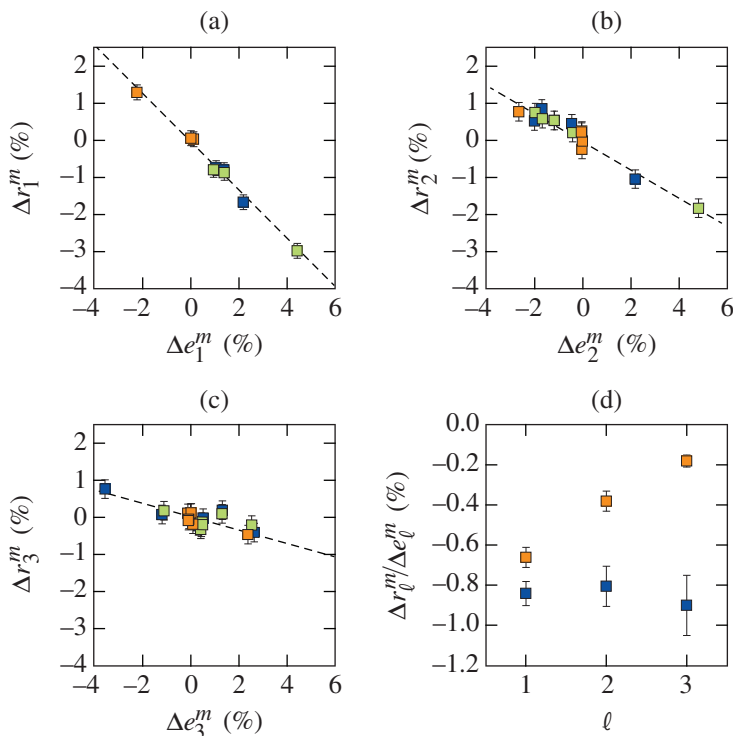

Figure 151.34
Comparison of the difference in the amplitude of the modes (a) $\ell = 1$, (b) $\ell = 2$, and (c) $\ell = 3$ of the ablation-front surface $\left(\Delta r_\ell^m\right)$ between shots 1 and 2 (orange points), 1 and 3 (blue points), and 2 and 3 (green points) with the difference in the corresponding modes in the laser-energy balance $\left(\Delta e_\ell^m\right)$. The linear fits are plotted in (a)–(c) as dashed black lines. (d) Comparison of C_ℓ (orange points) with C_ℓ/a_ℓ (blue points).

E26369JR

beam energies are balanced and the optimum laser-mode amplitudes that compensate them $[(e_{\text{opt}})_\ell^m]$. Over the three measurements $(r_{\text{res}})_\ell^m$ is obtained by averaging $(r_{\text{res}})_\ell^m = r_\ell^m - C_\ell e_\ell^m$ with an associated error of $\delta(r_{\text{res}})_\ell^m \approx \delta(r_\ell^m)/\sqrt{3} = \pm 0.05\%$; $(e_{\text{opt}})_\ell^m$ is given by $(e_{\text{opt}})_\ell^m = -(r_{\text{res}})_\ell^m / C_\ell$. Applying these corrected laser modes would lead to a spherical implosion with a maximum radial error

$$\approx \left\{ \sum_{\ell=0}^3 \sum_{m=-\ell}^\ell \left[\delta\left(\Delta r_\ell^m\right)^2 \right] \right\}^{0.5} = \pm 1\%.$$

In summary, tomographies of imploding shells were used to determine the laser energy balance that suppresses target modes $\ell = 1, 2,$ and 3. This is essential in direct-drive implosion experiments including ICF, where 3-D simulations predict significant enhancement in fusion performance.[8]

ACKNOWLEDGMENT

REFERENCES

1. R. P. Drake, *High-Energy-Density Physics: Fundamentals, Inertial Fusion, and Experimental Astrophysics, Shock Wave and High Pressure Phenomena* (Springer, Berlin, 2006).

2. A. L. Kritcher, T. Doeppner, D. Swift, J. Hawreliak, J. Nilsen, J. Hammer, B. Bachmann, G. Collins, O. Landen, C. Keane, S. Glenzer, S. Rothman, D. Chapman, D. Kraus, and R. W. Falcone, J. Phys.: Conf. Ser. **688**, 012055 (2016).

3. R. Nora, W. Theobald, R. Betti, F. J. Marshall, D. T. Michel, W. Seka, B. Yaakobi, M. Lafon, C. Stoeckl, J. A. Delettrez, A. A. Solodov, A. Casner, C. Reverdin, X. Ribeyre, A. Vallet, J. Peebles, F. N. Beg, and M. S. Wei, Phys. Rev. Lett. **114**, 045001 (2015).

4. A. B. Zylstra, J. A. Frenje, P. E. Grabowski, C. K. Li, G. W. Collins, P. Fitzsimmons, S. Glenzer, F. Graziani, S. B. Hansen, S. X. Hu, M. Gatu Johnson, P. Keiter, H. Reynolds, J. R. Rygg, F. H. Séguin, and R. D. Petrasso, Phys. Rev. Lett. **114**, 215002 (2015).

5. J. Nuckolls *et al.*, Nature **239**, 139 (1972).

6. O. A. Hurricane *et al.*, Nature **506**, 343 (2014).

7. S. P. Regan, V. N. Goncharov, I. V. Igumenshchev, T. C. Sangster, R. Betti, A. Bose, T. R. Boehly, M. J. Bonino, E. M. Campbell, D. Cao, T. J. B. Collins, R. S. Craxton, A. K. Davis, J. A. Delettrez, D. H. Edgell, R. Epstein, C. J. Forrest, J. A. Frenje, D. H. Froula, M. Gatu Johnson, V. Yu. Glebov, D. R. Harding, M. Hohenberger, S. X. Hu, D. Jacobs-Perkins, R. T. Janezic, M. Karasik, R. L. Keck, J. H. Kelly, T. J. Kessler,

J. P. Knauer, T. Z. Kosc, S. J. Loucks, J. A. Marozas, F. J. Marshall, R. L. McCrory, P. W. McKenty, D. D. Meyerhofer, D. T. Michel, J. F. Myatt, S. P. Obenschain, R. D. Petrasso, R. B. Radha, B. Rice, M. Rosenberg, A. J. Schmitt, M. J. Schmitt, W. Seka, W. T. Shmayda, M. J. Shoup, III, A. Shvydky, S. Skupsky, A. A. Solodov, C. Stoeckl, W. Theobald, J. Ulreich, M. D. Wittman, K. M. Woo, B. Yaakobi, and J. D. Zuegel, Phys. Rev. Lett. **117**, 025001 (2016); **117**, 059903(E) (2016).

8. I. V. Igumenshchev, V. N. Goncharov, F. J. Marshall, J. P. Knauer, E. M. Campbell, C. J. Forrest, D. H. Froula, V. Yu. Glebov, R. L. McCrory, S. P. Regan, T. C. Sangster, S. Skupsky, and C. Stoeckl, Phys. Plasmas **23**, 052702 (2016).

9. P. B. Radha, V. N. Goncharov, T. J. B. Collins, J. A. Delettrez, Y. Elbaz, V. Yu. Glebov, R. L. Keck, D. E. Keller, J. P. Knauer, J. A. Marozas, F. J. Marshall, P. W. McKenty, D. D. Meyerhofer, S. P. Regan, T. C. Sangster, D. Shvarts, S. Skupsky, Y. Srebro, R. P. J. Town, and C. Stoeckl, Phys. Plasmas **12**, 032702 (2005).

10. B. K. Spears, M. J. Edwards, S. Hatchett, J. Kilkenny, J. Knauer, A. Kritcher, J. Lindl, D. Munro, P. Patel, H. F. Robey, and R. P. J. Town, Phys. Plasmas **21**, 042702 (2014).

11. S. W. Haan *et al.*, Phys. Plasmas **18**, 051001 (2011).

12. A. Kritcher *et al.*, "Integrated Modeling of Cryogenic Layered High-Foot Experiments at the NIF," submitted to Physics of Plasmas.

13. D. S. Clark *et al.*, Phys. Plasmas **23**, 056302 (2016).

14. R. L. McCrory, R. E. Bahr, R. Betti, T. R. Boehly, T. J. B. Collins, R. S. Craxton, J. A. Delettrez, W. R. Donaldson, R. Epstein, J. Frenje, V. Yu. Glebov, V. N. Goncharov, O. Gotchev, R. Q. Gram, D. R. Harding, D. G. Hicks, P. A. Jaanimagi, R. L. Keck, J. Kelly, J. P. Knauer, C. K. Li, S. J. Loucks, L. D. Lund, F. J. Marshall, P. W. McKenty, D. D. Meyerhofer, S. F. B. Morse, R. D. Petrasso, P. B. Radha, S. P. Regan, S. Roberts, F. Séguin, W. Seka, S. Skupsky, V. Smalyuk, C. Sorce, J. M. Soures, C. Stoeckl, R. P. J. Town, M. D. Wittman, B. Yaakobi, and J. D. Zuegel, Nucl. Fusion **41**, 1413 (2001).

15. V. N. Goncharov, S. P. Regan, E. M. Campbell, T. C. Sangster, P. B. Radha, J. F. Myatt, D. H. Froula, R. Betti, T. R. Boehly, J. A. Delettrez, D. H. Edgell, R. Epstein, C. J. Forrest, V. Yu. Glebov, D. R. Harding, S. X. Hu, I. V. Igumenshchev, F. J. Marshall, R. L. McCrory, D. T. Michel, W. Seka, A. Shvydky, C. Stoeckl, W. Theobald, and M. Gatu-Johnson, Plasma Phys. Control. Fusion **59**, 014008 (2017).

16. K. Molvig *et al.*, Phys. Rev. Lett. **116**, 255003 (2016).

17. C. K. Li, F. H. Séguin, J. A. Frenje, R. D. Petrasso, J. A. Delettrez, P. W. McKenty, T. C. Sangster, R. L. Keck, J. M. Soures, F. J. Marshall, D. D. Meyerhofer, V. N. Goncharov, J. P. Knauer, P. B. Radha, S. P. Regan, and W. Seka, Phys. Rev. Lett. **92**, 205001 (2004).

18. T. J. Murphy, Phys. Plasmas **21**, 072701 (2014).

19. J. J. Ruby, A. Pak, J. E. Field, T. Ma, B. K. Spears, L. R. Benedetti, D. K. Bradley, L. F. Berzak Hopkins, D. T. Casey, T. Döppner, D. Eder, D. Fittinghoff, G. Grim, R. Hatarik, D. E. Hinkel, N. Izumi, J. D. Kilkenny, S. F. Khan, J. P. Knauer, A. L. Kritcher, F. E. Merrill, J. D. Moody, S. R. Nagel, H.-S. Park, J. D. Salmonson, D. B. Sayre, D. A. Callahan, W. W. Hsing, O. A. Hurricane, P. K. Patel, and M. J. Edwards, Phys. Plasmas **23**, 072701 (2016).

20. R. C. Shah, B. M. Haines, F. J. Wysocki, J. F. Benage, J. A. Fooks, V. Glebov, P. Hakel, M. Hoppe, I. V. Igumenshchev, G. Kagan, R. C. Mancini, F. J. Marshall, D. T. Michel, T. J. Murphy, M. E. Schoff, K. Silverstein, C. Stoeckl, and B. Yaakobi, Phys. Rev. Lett. **118**, 135001 (2017).

21. P. Michel *et al.*, Phys. Plasmas **17**, 056305 (2010).

22. G. A. Kyrala *et al.*, Phys. Plasmas **18**, 056307 (2011).

23. R. P. J. Town, D. K. Bradley, A. Kritcher, O. S. Jones, J. R. Rygg, R. Tommasini, M. Barrios, L. R. Benedetti, L. F. Berzak Hopkins, P. M. Celliers, T. Döppner, E. L. Dewald, D. C. Eder, J. E. Field, S. M. Glenn, N. Izumi, S. W. Haan, S. F. Khan, J. L. Kline, G. A. Kyrala, T. Ma, J. L. Milovich, J. D. Moody, S. R. Nagel, A. Pak, J. L. Peterson, H. F. Robey, J. S. Ross, R. H. H. Scott, B. K. Spears, M. J. Edwards, J. D. Kilkenny, and O. L. Landen, Phys. Plasmas **21**, 056313 (2014).

24. R. Tommasini, S. P. Hatchett, D. S. Hey, C. Iglesias, N. Izumi, J. A. Koch, O. L. Landen, A. J. MacKinnon, C. Sorce, J. A. Delettrez, V. Yu. Glebov, T. C. Sangster, and C. Stoeckl, Phys. Plasmas **18**, 056309 (2011).

25. H. M. Johns, R. C. Mancini, T. Nagayama, D. C. Mayes, R. Tommasini, V. A. Smalyuk, S. P. Regan, and J. A. Delettrez, Phys. Plasmas **23**, 012709 (2016).

26. D. T. Michel, A. K. Davis, W. Armstrong, R. Bahr, R. Epstein, V. N. Goncharov, M. Hohenberger, I. V. Igumenshchev, R. Jungquist, D. D. Meyerhofer, P. B. Radha, T. C. Sangster, C. Sorce, and D. H. Froula, High Power Laser Sci. Eng. **3**, e19 (2015).

27. R. S. Craxton, K. S. Anderson, T. R. Boehly, V. N. Goncharov, D. R. Harding, J. P. Knauer, R. L. McCrory, P. W. McKenty, D. D. Meyerhofer, J. F. Myatt, A. J. Schmitt, J. D. Sethian, R. W. Short, S. Skupsky, W. Theobald, W. L. Kruer, K. Tanaka, R. Betti, T. J. B. Collins, J. A. Delettrez, S. X. Hu, J. A. Marozas, A. V. Maximov, D. T. Michel, P. B. Radha, S. P. Regan, T. C. Sangster, W. Seka, A. A. Solodov, J. M. Soures, C. Stoeckl, and J. D. Zuegel, Phys. Plasmas **22**, 110501 (2015).

28. I. V. Igumenshchev, D. T. Michel, R. C. Shah, E. M. Campbell, R. Epstein, C. J. Forrest, V. Yu. Glebov, V. N. Goncharov, J. P. Knauer, F. J. Marshall, R. L. McCrory, S. P. Regan, T. C. Sangster, C. Stoeckl, A. J. Schmitt, and S. Obenschain, Phys. Plasmas **24**, 056307 (2017).

29. D. T. Michel, C. Sorce, R. Epstein, N. Whiting, I. V. Igumenshchev, R. Jungquist, and D. H. Froula, Rev. Sci. Instrum. **83**, 10E530 (2012).

30. T. R. Boehly, D. L. Brown, R. S. Craxton, R. L. Keck, J. P. Knauer, J. H. Kelly, T. J. Kessler, S. A. Kumpan, S. J. Loucks, S. A. Letzring, F. J. Marshall, R. L. McCrory, S. F. B. Morse, W. Seka, J. M. Soures, and C. P. Verdon, Opt. Commun. **133**, 495 (1997).

31. T. R. Boehly, V. A. Smalyuk, D. D. Meyerhofer, J. P. Knauer, D. K. Bradley, R. S. Craxton, M. J. Guardalben, S. Skupsky, and T. J. Kessler, J. Appl. Phys. **85**, 3444 (1999).

32. S. Skupsky, R. W. Short, T. Kessler, R. S. Craxton, S. Letzring, and J. W. Soures, J. Appl. Phys. **66**, 3456 (1989).

33. T. J. Kessler, Y. Lin, J. J. Armstrong, and B. Velazquez, Proc. SPIE **1870**, 95 (1993).

34. E. T. Whittaker and G. N. Watson, *A Course of Modern Analysis* (Cambridge University Press, 1927), p. 392.

35. D. K. Bradley, P. M. Bell, J. D. Kilkenny, R. Hanks, O. Landen, P. A. Jaanimagi, P. W. McKenty, and C. P. Verdon, Rev. Sci. Instrum. **63**, 4813 (1992).

36. D. T. Michel, V. N. Goncharov, I. V. Igumenshchev, R. Epstein, and D. H. Froula, Phys. Rev. Lett. **111**, 245005 (2013).

37. D. T. Michel, S. X. Hu, A. K. Davis, V. Yu. Glebov, V. N. Goncharov, I. V. Igumenshchev, P. B. Radha, C. Stoeckl, and D. H. Froula, Phys. Rev. E **95**, 051202(R) (2017).

38. H. L. Seal, Biometrika **54**, 1 (1967).

39. S. Skupsky and K. Lee, J. Appl. Phys. **54**, 3662 (1983).

40. L. Spitzer, Jr. and R. Härm, Phys. Rev. **89**, 977 (1953).